ETHzürich

Tuning Electron-Phonon Interactions in Nanocrystals through Surface Termination

Tuning Electron-Phonon Interactions in Nanocrystals through Surface Termination

Nuri Yazdani1, Deniz Bozyigit1, Kantawong Vuttivorakulchai2, Mathieu Luisier2, Ivan Infante3, Vanessa Wood1*

1 Labratory for Nanoelectronics, Department of Information Technology and Electrical Engineering, ETH Zurich, CH-8092 Switzerland,

2 Nano TCAD Group, Department of Information Technology and Electrical Engineering, ETH Zurich, CH-8092 Switzerland

3 Division of Theoretical Chemistry and Amsterdam Center for Multiscale Modeling (ACMM), Vrije University Amsterdam, De Boelelaan 1083, 1081 HV Amsterdam, The Netherlands

Nanocrystals, quantum dots, phonons, electron-phonon coupling, thermal broadening, carrier cooling

Abstract

We perform *ab initio* molecular dynamics (AIMD) on experimentally-relevant sized lead sulfide (PbS) nano-crystals (NCs) constructed with thiol or Cl, Br, and I anion surfaces to determine their vibrational and dynamic electronic structure. We show that electron-phonon interactions can explain the large thermal broadening and fast carrier cooling rates experimentally observed in Pb-chalcogenide NCs. Furthermore, our simulations reveal that electron-phonon interactions are suppressed in halide terminated NCs due to reduction of both the thermal displacement of surface atoms and the spatial overlap of the charge carriers with these large atomic vibrations. This work shows how surface engineering – guided by simulations – can be used to systematically control carrier dynamics.

The efficiency of nanocrystal (NC)-based optical, optoelectronic, and electronic devices has benefitted tremendously from advances in NC surface chemistry.[1,2] High photo-luminescent quantum yields in NCs are linked to engineering of the NC surface, where core/shell structures have been used[3] to optimize radiative rates,[4] emission wavelengths,[5] and hot carrier cooling rates.[6] NC-based solar cell performance has been improved with the evolution of termination strategies to increase charge carrier mobility,[7,8] reduce charge carrier recombination,[9] and increase carrier extraction through optimizing inter-NC band alignment.[10] Recently, it has become clear that the surface of the NC plays an important role in electron-phonon coupling,[11] which is key to determining their dynamic electronic and optical properties, including charge transport, non-radiative recombination, homogeneous broadening of optical transitions, and intra-band carrier relaxation.

Here we perform Ab-Initio Molecular Dynamics (AIMD) and semi-classical stochastic surface hopping calculations on experimentally relevant sized NCs to investigate phonon-mediated optical and electronic transitions and how the strength of the electron-phonon interactions can be tuned through surface engineering of the NC. AIMD generates the nuclear dynamics of the NC within the adiabatic approximation, while the forces on the nuclei are calculated at each time step with the electronic structure obtained with density functional theory (DFT). AIMD thus provides the dynamic adiabatic electronic structure along with the nuclear trajectories. The phonon spectra of the NCs can be determined from the nuclear dynamics, and phonon coupling to electronic and optical transitions can be calculated utilizing the dynamic adiabatic electronic structure. Thermal broadening of optical transitions can be quantified from the time-dependent state energies, while semi-classical stochastic surface hopping calculations over the adiabatic energy surfaces mapped out by the AIMD can be employed to simulate charge carrier dynamics, in particular, the cooling of hot carriers.

We choose to work with lead sulfide (PbS) NC due to the large amount of data on their electronic and optical properties and their use in a wide variety of bottom-up fabricated opto-electronic devices.[12] We construct PbS NCs with a radius of $r = {\sim}1.2$ nm, following the atomistic model proposed by Zherebetskyy *et al.*[13] (see **Supporting Information SI-1**). The NCs consist of $N_{Pb}=201$ lead atoms, $N_S=140$ sulfur atoms, and the Pb-rich [111] surfaces are terminated with ligands. To capture the chemistry of the Pb-S bond present in thiol-terminated NCs, such as ethane-dithiol (EDT) or 3-mercaptopropionic acid (MPA), which are used for NC devices,[14–16] a methane-thiol (mth) ligand is selected.

We first investigate this thiol-terminated PbS NC. The fully geometrically relaxed NC is shown in **Figure 1a**. As expected for an defect-freeNC, no states are found in the bandgap, and a larger density of states is present in the valence band ($3p$-S / $6s$-Pb character) than in the conduction band ($6p$-Pb / $3s$-S character), which is consistent with calculations on PbSe NCs.[17] The 4-fold degeneracy of the valence band maximum (VBM) and conduction band minimum (CBM) in bulk-PbS is broken due to inter-valley coupling[17–20] resulting from the [100] facets of the NCs. The conduction band minimum is singly degenerate (which we label ψ_{1e}) followed by triply degenerate states ($\psi_{2e\alpha}$) split by 143meV for the PbS/mth NC, while the valence band maximum is triply degenerate ($\psi_{1h\alpha}$) followed by a singly degenerate state (ψ_{2h}), with a 142meV splitting. We also find that the lowest energy transitions (the three fold degenerate $\psi_{1h\alpha} \rightarrow \psi_{1e}$) are weakly optically coupled, while the higher energy $\psi_{1h\alpha} \rightarrow \psi_{2e\alpha}$ transitions are more strongly optically coupled, i.e. responsible for the first absorption peak. This is consistent with the observation of large difference between the emission and first absorption peak for PbS NCs.[21] Further details about the electronic and optical structure of the NC and of bulk PbS are given in the **Supporting Information SI-2-3**.

We perform AIMD simulations over 10-15 ps on the NC at three different temperatures: 0 K, 100 K, and 300 K. Videos showing the time evolution of the atomic positions, the

conduction band minimum wavefunction, and the carrier density in the valence band maximum over a 1ps time window are provided as **Supplemental Movie 1 and 2**. In **Figure 1b**, the time dependent state energies at 300K are plotted, in which large non-coherent fluctuations are evident. The strong fluctuations of the carrier densities and state energies, and their increase with temperature, is a clear indication of the dependence of the electronic structure on the nuclear coordinates of the NCs, indicative of electron-phonon coupling.

The AIMD and surface hopping calculations enable us to computationally study two experimentally observed, but until now not fully understood, properties of Pb chalcogenide NCs - (1) large thermal broadening and (2) fast carrier cooling. We first show that our simulations provide values that are in good agreement with experiment, and then analyze the AIMD results to explain the origins of these phenomena.

Large thermal broadening is a typical feature of colloidal NCs,[22–24]with room temperature linewidths exceeding 10% of the NC bandgap for smaller NCs,[25,26]   While electron-phonon coupling is expected to play a role in thermal broadening,[24,27–29] the large linewidth in PbS NCs had led to some studies to attribute it to multiple emissive states.[26] To determine the expected thermal broadening from electron-phonon coupling, we consider the time dependence of lowest energy transition, nominally three-fold degenerate, (indicated by the arrows in **Figure 1b**):

$$E_g(t) = E_{1e}(t) - E_{1h\alpha}(t). \tag{1}$$

A histogram of the E_g values at 10K, 100K, and 300K are shown in **Figure 1c**. The $E_g(t)$ distributions broaden and red shift with increasing temperature. From the width of the distributions, we extract a thermal broadening which increases with temperature from σ_{Eg}(10K)=13meV to σ_{Eg}(100K)=31meV and σ_{Eg}(300K)=72meV, where σ_{Eg} corresponds to the standard deviation of the distributions. The values agree well with recent measurements on emission spectra of single PbS NCs (65meV $< \sigma(r{\sim}1.2nm) <$ 100meV)[26] and isotypic PbSe

NCs ($\sigma(r{\sim}1.4nm){\sim}50meV$, $\sigma(r{\sim}0.95nm){\sim}100meV$).[25] This indicates that the experimentally observed linewidths in PbS NCs result primarily from the energy fluctuations of the lowest energy transition that stems from the nuclear dynamics in NCs. We note that the linewidths calculated here represent a lower limit. As we show in the **Supporting Information SI-2**, loss of the octahedral symmetry of the NC will split the degeneracy of the lowest energy transition, $\psi_{1h\alpha} \rightarrow \psi_{1e}$, resulting in an increased luminescence linewidth.

Recent experimental[11,30–36] and theoretical[37–40] work have also indicated that electron-phonon coupling enables efficient, thermally activated, multi-phonon-mediated[11,30,41] electronic transitions. For lead-chalcogenide NCs, sub-picosecond time constants have been measured for intra-band carrier cooling.[42–44] To investigate carrier cooling driven by multi-phonon-mediated electronic transitions, we consider the non-adiabatic transition probability between state i and j, which depends on the non-adiabatic coupling,[45,46]

$$d_{i,j} = -i\hbar \left\langle \psi_i(t) \left| \frac{\partial}{\partial t} \right| \psi_j(t) \right\rangle. \tag{2}$$

This coupling will become large about the avoided crossing between state i and j along the adiabatic state energy surfaces (refer to **Figure 1b** for an example). To simulate the carrier dynamics, we employ semi-classical stochastic surface hopping calculations[46] over the adiabatic energy surfaces mapped out by the AIMD. In particular, we use the fewest switches surface hopping within the neglect of back reactions approximation (FSSH-NBRA), described in detail in Ref. [45], employed by Kilina and coworkers in the study of small CdSe and PbSe clusters.[38,47] FSSH-NBRA stochastically generates time dependent state occupation probabilities, $n_i(t)$, by propagating initial state occupations according to the non-adiabatic transition probabilities of eq. (2), weighted by the Boltzmann factor to maintain detailed balance.[37,45,46] From the simulated $n_i(t)$, we calculate the time dependent occupation weighted density of states,

$$p(E,t) = \sum_i n_i(t)\delta\big(E_i(t) - E_R(t)\big), \tag{3}$$

where δ is the Dirac delta function, $E_i(t)$ is the energy of state i at time t, and $E_R(t)$ is a reference state energy. In **Figure 1d**, we plot the dynamics of $p(E,t)$ for an electron relaxing in the conduction band and a hole relaxing in the valence band, both initially excited to a state with mean energy ~0.5eV above the band edges. Superimposed on the plot is the trace of the average carrier energy,

$$\langle E(t)\rangle = \int p(E,t)EdE, \tag{4}$$

along with an exponential fit of the form

$$\langle E(t)\rangle \propto e^{-t/t_0}, \tag{5}$$

where t_0 is the time constant associated with the excess energy loss of the carrier. For this initial excited state with mean excess energy of 0.5eV, we find that electrons cool with a time constant $t_{0,e}$~825fs, while holes cool significantly faster with a time constant $t_{0,e}$~182fs, corresponding to initial energy loss rates of 0.6eV/ps and 2.7eV/ps, respectively. These cooling rates are consistent with recent measurements on isotypic PbSe NCs with 0.54eV/ps and 2.75eV/ps for electrons and holes respectively[43,44] (see **Supporting Information SI-5** for time constants associated with the build-up of carrier population of holes in the $\psi_{1h\alpha}$ states and electrons in the ψ_{1e} state).

Additional insight into carrier cooling can be obtained by considering the average coupling of the carrier to transitions (eq. (2)). To do so, we compute the wavefunction overlap correlation function, $R_{i,j}(\tau) = \left\langle \left|\langle\psi_i(t)|\psi_j(t+\tau)\rangle\right|^2 \right\rangle_t$, where $<...>_t$ represents an averaging over the time trace of the AIMD. The average coupling to a transition can be related to the time-derivative of the correlation function:

$$\left\langle d_{i,\mathrm{j}} \right\rangle_{t} = -i\hbar \frac{\partial}{\partial \tau} \left\langle \left\langle \psi_{i}(t) \middle| \psi_{j}(t+\tau) \right\rangle \right\rangle_{t} \Bigg|_{\tau=0}$$

$$\equiv -i\hbar \frac{1}{2} \frac{\partial}{\partial \tau} \left[R_{i,j}(\tau) - \sigma^{2} \left[\left\langle \psi_{i}(t) \middle| \psi_{j}(t+\tau) \right\rangle \right] \right] \Bigg|_{\tau=0} \qquad (6)$$

$$\approx -i\hbar \frac{1}{2} \frac{\partial}{\partial \tau} R_{i,j}(\tau) \Bigg|_{\tau=0} ,$$

where we have defined $R_{ij}(\tau) = <<\psi_i(t)|\psi_j(t+\tau)>^2>_t$ and the last step follows as we find the variance of $<\psi_i(t)|\psi_j(t+\tau)>$ to be small (see **Supporting Information SI-6**). Rather than considering all possible transitions for a carrier into the conduction band minimum or valence band maximum, we can focus on the *auto*-correlation function associated with a carrier in one of the band extrema, $R_{ii}(\tau)$, which, due to completeness, is related to the sum of average couplings to all possible transitions:

$$\sum_{i\neq j} \left\langle d_{i,j} \right\rangle_{t} \approx -i\hbar \sum_{i\neq j} \frac{1}{2} \frac{\partial}{\partial \tau} R_{i,j}(\tau) \Bigg|_{\tau=0} = i\hbar \frac{1}{2} \frac{\partial}{\partial \tau} R_{i,i}(\tau) \Bigg|_{\tau=0}. \qquad (7)$$

We therefore compute:

$$R_{CBM}(\tau) = \left\langle \left| \left\langle \psi_{1e}(t) \middle| \psi_{1e}(t+\tau) \right\rangle \right|^{2} \right\rangle_{t} ,$$

$$R_{VBM}(\tau) = \frac{1}{3} \sum_{\alpha,\beta} \left\langle \left| \left\langle \psi_{1h\alpha}(t) \middle| \psi_{1h\beta}(t+\tau) \right\rangle \right|^{2} \right\rangle_{t} . \qquad (8)$$

As the valence band maximum is nominally three-fold degenerate, we evaluate the average coupling associated with the carrier remaining in one of the $\psi_{1h\alpha}$ states. An auto-correlation function $R_{ij}(\tau)$ that rapidly deviates from unity implies rapid dephasing of the wavefunction away from the state i and therefore a strong coupling to transitions to/from state i. Plots of $R_{CBM}(\tau)$ and $R_{VBM}(\tau)$ are presented in **Figure 1e.** Consistent with picture that electronic transitions to these states are driven by multi-phonon emission, the mean coupling of transitions from the band extrema increase for both bands with increasing temperature. The results also indicate stronger coupling of transitions with the valence band maximum compared to the

conduction band minimum, in agreement with the results from the surface hopping calculations presented above, which showed faster carrier cooling to the valence band maximum than the conduction band minimum.

To determine which phonon modes in the NC are responsible for the large thermal broadening and fast carrier cooling, we first compute the phonon density of states, $g(\omega)$, of the NC. It can be obtained from the power spectrum of the mass-weighted position correlation function, $r_i(t)$:[48]

$$g_i(\omega) = m_i\omega^2 \left|\mathcal{F}\{r_i(t)\}\right|^2, \quad g(\omega) = \sum_i g_i(\omega), \qquad (9)$$

where m_i is the mass of atom i. **Figure 2a** shows the total $g(\omega)$ (black), which is in good agreement with experimental measurements of the $g(\omega)$ on thiol terminated PbS NCs using inelastic neutron scattering.[11] We then calculate the power spectral density of the time dependent bandgap, $\left|\mathrm{F}\left[E_g(t)\right]\right|^2$ (**Figure 2b**), and the power spectral density of the wavefunction overlap autocorrelation functions (eq. (8)), $\left|\mathrm{F}\left[R(\tau)\right]\right|^2$ (**Figure 2c**), where $\mathcal{F}$ represents a Fourier transform. A peak in the power spectral density at a specific frequency indicates that phonons at that frequency actively drive the fluctuations in state energies and induce thermal broadening or wavefunction dephasing. The power spectral densities all indicate that electrons couple to both low energy modes (5-40cm-1), below the transverse acoustic peak (48.8cm-1 for bulk PbS), as well as to high energy optical phonons, (150-250cm-1). The electron-phonon coupling to two distributions of modes is in agreement with previous work,[11] where it was shown experimentally that large energy multi-phonon-mediated electronic transitions were driven by both low (25-40cm-1) and high (120-240cm-1) energy phonons.

To determine which atoms in the NCs contribute to the modes coupling to these processes, we plot the partial $g(\omega)$ for atoms located in three different regions in the NC (**Figure 2d**). As we previously reported,[11] in the core of the NCs (Region 3), the partial $g(\omega)$ resembles

that of bulk PbS while deviations from the bulk PbS $g(\omega)$ arise due to the outer atomic layers of the NC (Region 1). The low energy phonon modes couple to optical and electronic transitions and are primarily confined to the outer surface of the NC.

The high frequency modes coupling to transitions to/from the valence band maximum are localized vibrations of the S atoms on the surface of the NC. A higher hole density on the surface S atoms in the VBM (~0.20) compared to the CBM (0.06), can then explain the stronger coupling of these modes to the VBM (see **fig. 2c**). The faster hole cooling observed therefore stems from not only a higher density of states in the VB, but additionally from stronger coupling to vibrations on the surface of the NC.

These findings highlight that surface atoms play an important role in electron-phonon coupling and that changing the NC surface could be a practical method to control electron-phonon interactions in NCs and thereby tune optical properties such as the thermal broadening and carrier cooling rates. We therefore systematically investigate the influence of surface termination on electron-phonon coupling by constructing NCs with I, Br, Cl ligands and repeating the AIMD and stochastic surface hopping calculations described above.

We first compare results of the thiol terminated NC (PbS/mth) with a Cl terminated NC (PbS/Cl). **Figure 3a** shows that the thermal broadening is reduced in the PbS/Cl NC compared to the PbS/mth NC, with a ~30% reduction at 300K. This finding is consistent with the decrease of the thermal broadening upon halide passivation that has been demonstrated experimentally.[21] Likewise, energy loss rates for holes in the valence band is consistently slower (<1/2x) for the PbS/Cl NC than for the PbS/mth NC (**Figure 3b)**. For electrons in the CB, cooling rates are significantly slower (<1/4x) for the PbS/Cl NC than the PbS/mth NC in the case of excitation to states with low initial excess energies (e.g., 0.1 eV-0.2 eV), while, with excitations to states with large excess energies (> 0.6 eV), the cooling rates are similar for both the PbS/Cl and PbS/mth NC. This implies that carrier cooling at high excess energies in the

conduction band is similar in both the PbS/Cl and PbS/mth NCs, consistent with bulk-like cooling rates at high excess energies measured by Spoor *et al.* in PbSe,[44] while PbS/Cl NCs exhibit comparatively slow electron cooling from the $\psi_{2e\alpha}$ states to ψ_{1e} (**Supporting Information SI-7**).

To demonstrate that the reduced thermal broadening and the slower carrier cooling stem from reduced electron phonon coupling, we compare the spectral densities of the mth- and Cl-terminated NCs (**Figure 3c**). We find that the reduction in thermal broadening for halide terminated NCs stems from a significant reduction in coupling to the optical phonon modes, as well as a reduction in the coupling to the lower energy modes. Integrating the power spectra, we find an overall reduction of ~50%, consistent with the reduction in extent of thermal broadening $((1-0.30)_2 \sim 0.50)$. Similarly, the plots of $\left| F\left[R(\tau) \right] \right|^2$ for the valence band maximum and conduction band minimum indicate that the slower cooling results from a decrease in the coupling to both low and high energy modes, with an ~60% decrease in the integrated power spectra for both.

To understand the origins of the decreased coupling of phonons to optical and electronic transitions upon halide passivation, we complement the calculations on mth- and Cl-terminated NCs with calculations on Br and I surface terminated PbS NCs. If we extract the thermal broadening at 100K for all four surface terminations (σ_{Eg}(100K)=31meV for PbS/mth, 27meV for PbS/I, 26meV for PbS/Br, and 25meV for PbS/Cl), we find that it decreases with increasing effective electronegativity of the surface termination (**Table 1**). In **Figure 4a**, we plot the sum of the mean coupling constants $(-i\hbar)^{-1} \sum_{i \neq j} \left\langle d_{ij} \right\rangle_t$ for transitions from (or to) the conduction band minimum and valence band maximum for all four surface terminations. Again, the coupling constants decrease with an increase in electronegativity. Both these results indicate a

decrease in electron-phonon coupling with an increase in effective electronegativity of the ion or binding group that coordinates the [111] surface.

In order to understand the origin of this decrease in electron-phonon coupling, we systematically analyze the vibrational and electronic structure of the NCs with the four different surface terminations. A typical approach to estimate the strength of coupling of phonons to optical or electronic transitions is to compute the dimensionless Huang-Rhys factor, S_{HR}. The latter can be approximated by:

$$S_{HR} = A \times M \times \left\langle u^2 \right\rangle \times \left(k_B T \right)^{-1} \times \left(\hbar \omega \right)^{-1} \times D^2, \qquad (10)$$

where A is the unit-less overlap integral of the electronic states with M number of phonon modes with frequency ω, D the deformation potential in (eV/Å), and $<u_{\omega 2}>$ is the mean square thermal displacement of the modes (Å2).[49] From expression (10), we expect that a change in electron-phonon coupling for a specific electronic transition and phonon mode can result from a change in (1) the number and frequency of available phonons, which would be reflected in a change in the density of states $g(\omega)$, (2) the thermal displacement of the atoms contributing to phonon mode of the given frequency, or (3) the overlap between the electronic wavefunction and the given vibrational mode.

First, we compare the $g(\omega)$ for the different NC surface terminations (**Supporting Information SI-8**). All NCs exhibit modes from Pb-atoms that are lower in frequency than TA peak in bulk PbS, and the small deviations in the $g(\omega)$ cannot explain the differences in electron-phonon coupling observed for the different terminations.

However, the second parameter playing a role in electron-phonon coupling, $<u_2>$, shows systematic changes as a function of the NC surface termination. The $<u_2>$ at 100K for the Pb, S, and halide anion atoms in the three NC regions are plotted in **Figure 4b**. Values for Pb and S calculated for bulk PbS are provided for reference (black lines). Three trends are

evident. First, the further away a Pb or S atom is from the surface, the smaller its $<u_2>$ value. In the core of the NC (Region 3), the $<u_2>$ values for Pb or S are similar to those in bulk PbS. Second, the $<u_2>$ values for the Pb and S atoms at the surface are smaller for PbS NCs with halide terminations than for the PbS/mth NC. Third, very large $<u_2>$ are observed for anions (S, I, Br, and Cl) on the [111] surface facets. These three observations can be explained by recalling that atomic displacement is inversely related to the effective spring constant of the phonon mode, κ_{eff}, [Ref. 11]:

$$\left\langle u^2 \right\rangle = k_B T / \kappa_{eff}. \qquad (11)$$

κ_{eff} is associated with the bonding strength between neighboring atoms. Pb and S atoms in the interior of a NC have a coordination number of 6, while the surface Pb and S atoms on the [100] facets of the NCs have a coordination number of 5, and surface anions such as S, I, Br, and Cl on the [111] facets have a coordination numbers of 2 or 3 (ignoring the S-C bonds in the PbS/mth NC). Thus, larger $<u_2>$ are linked to decreased coordination number. Furthermore, the large $<u_2>$ of the Pb atoms on the outermost [111] facet for PbS/mth NC compared to halide terminated NCs can be explained by the strength of the bond. The effective spring constants associated with the Pb-X (X=mth, I, Br, Cl) bonds with the [111] surface atoms should scale with the percentage ionic character of the bonds,[50] and the decrease in $<u_2>$ with the increase in ligand electronegativity is therefore expected (**Table 1**).

Finally, we consider the overlap between the electronic wavefunction and the given vibrational mode. In **Figure 4c**, we plot cross-sections of the electron density for the VBM and CBM for NCs with the different surface terminations. The extent of electronic confinement increases with increasing electronegativity of the anion (S, I, Br, Cl), which is also evidenced by the increasing electronic bandgaps (**Table 1**). Consistent with previous calculations on Cl-terminated NCs,[51] the wavefunctions for our halide-terminated NCs are confined away from the [111] facets. The total carrier density,

$$p_{n,surf.} = \sum_{\langle i \rangle, \sigma} \left| \varphi_{n,i\sigma} \right|^2 , \qquad (12)$$

where i runs over the two outermost atomic layers on the [111] facet, and $\varphi_{n,i\sigma}$ are the components of the n_{th} wavefunction projected onto the atomic orbitals σ of the i_{th} atom, decreases by 40% (0.17→0.10) in the conduction band minimum and 60% (0.27→0.11) in the valence band maximum by replacing the mth with Cl.

We therefore conclude that electron-phonon interactions are reduced in halide terminated NCs compared to thiol-terminated NCs due to (1) reduction of the mean square displacement of Pb and S atoms in the NC and (2) confinement of the conduction and valence band wavefunctions away from the [111] surface where the largest atomic displacement modes occur. To quantify this, we propose the parameter A_{ue}, which we define as the overlap of the carrier density with the mean thermal displacement of the atoms:

$$A_{ue} = \sum_i \left[\left\langle u_i^2 \right\rangle \sum_\sigma \left| \varphi_{n,i\sigma} \right|^2 \right], \qquad (13)$$

where i runs over all atoms in the NC. The A_{ue} at 100K for the conduction band minimum and valence band maximum for the four different surface terminations are tabulated in **Table 1**. The Cl-terminated NCs reveal a > 40% reduction in A_{ue} for the band extreme compared with the mth-terminated NC and values that approach about 90% of the value for bulk PbS.

Lastly, we investigate the impact of carboxylate surface termination, PbS/COO, being the most common termination for spectroscopic studies of PbS, here we employ acetic acid for computational efficiency. After a full geometry relaxation of the NC, the ligands bind in either a bridging or chelating bidentate geometry as expected from NMR studies,[52] as shown in **Figure 5a**. The expected thermal broadening at 300K is shown in **Figure 5b**, and we find the broadening to between that of PbS/mth and PbS/Cl: σ_{Eg}(mth,300K) = 72meV > σ_{Eg}(COO,300K) = 60meV > σ_{Eg}(Cl,300K) = 50meV. Plots of the auto-correlation functions,

eq. (8), for the PbS/COO at 300K are shown in **Figure 5c**, along with those for PbS/mth and PbS/Cl for reference. Interestingly, we find the average coupling to the CBM, eq. (7), to be approximately equal to Cl termination, so we can expect electron cooling rates similar to the those found for Cl termination. On the other hand, the average coupling to the VBM is approximately equal to thiol termination, indicating cooling rates for holes similar to thiol termination for hydroxylate termination.

In summary, our calculations indicate that strong thermal broadening and fast carrier cooling observed in lead-chalcogenide NCs are intrinsic effects resulting from strong coupling of charge carriers and phonons in the NC, particularly modes arising from the surface atoms of the NCs. While we do not rule out that these processes can be affected by emission from defect states,[26] long range energy transfer to ligand or solvent vibrations,[6] or energy loss through Auger processes in highly charged NCs,[34,36] we find that these additional effects are not necessary to explain experimental observations in lead-chalcogenide NCs. We have further demonstrated that the strength of electron phonon coupling can be tuned in the NCs through engineering of the surface termination. In particular, electron-phonon coupling in NC can be suppressed by reducing the mean thermal displacement of atoms and the overlap of the electronic density with atoms having a large thermal displacement. Our findings provide a new lever of control for these systems for application-specific material optimization.

Methods

Construction of NCs

The approach used for the construction of the NCs investigated in this work is shown schematically in Figure S1. To construct the NCs, bulk rocksalt PbS (with a Pb or S atom centered on the origin) is cut along the eight (111) planes and six (100) planes at plane to origin distances (r) defined by the Wulff ratio Rw

$$r_{(1,0,0)} = AR_W, \quad r_{(1,1,1)} = AR_W^{-1}. \qquad (14)$$

The scalar A is adjusted such that the resulting NC is S-terminated on the (111) facets. These (111)-surface terminating S atoms are then replaced with the desired ligand. To obtain an intrinsic semiconductor NC, overall charge balance must be maintained. This includes contributions from the ligands and charging of the NC compensated by counter-ions in solution,[51,53]

$$\begin{aligned} N_{e(cat)} - N_{e(an)} &= 0, \\ 2N_{Pb} - 2N_S + N_L V_L + N_{ch}e &= 0, \end{aligned} \qquad (15)$$

where N_x refers to the number of Pb or S atoms, ligands (L), or surplus/deficiency of additional charges (ch), and V_L is the valence of the ligand.

For a range of NC radii (~1nm to ~2nm), taking $Rw = 0.82$ and using thiol or halide anion ligands ($V_L = -1$), the charge balance condition (Equation 1.1) is almost satisfied ($\leq \pm 2e$). NCs cut with Rw other than 0.82 require the removal of far more (typically >10) ligands/Pb-ligand-pairs or strong charging in order to satisfy eq. (15). For the case $Rw = 0.82$, to fully satisfy eq. (15), one to two ligands (-) or Pb-ligand-pairs (+) are removed. Alternatively, the NC can assume to be charged ($N_{ch} = \pm 1/\pm 2$). In contrast to the case of ligand removal, with charged NCs retain octahedral symmetry. All of the NCs studied in this work are charged by +2e.

Simulations

Geometry optimization, electronic structure calculations, and *ab initio* molecular dynamics (AIMD) are performed within the CP2K program suite utilizing the quickstep module.[54] Calculations are carried out using a dual basis of localized Gaussians and plane-waves,[55] with a 300Ry plane-wave cutoff. As in previous calculations for CdSe[56] and PbS[11] NCs, Double-Zeta-Valence-Polarization (DZVP),[57] Goedecker–Teter–Hutter pseudopotentials[58] for core electrons, and the Perdew–Burke–Ernzerhof (PBE) exchange correlation functional are used

for all calculations. Convergence to 10_{-8} in Self-Consistent Field calculations is always enforced.

For NCs, non-periodic boundary conditions are used, and 4nmx4nmx4nm cubic unit cells are defined for the $r=1.2$nm NCs. For bulk PbS calculations, periodic boundary conditions for the 4x4x4 cubic supercell (512 atoms) are applied, and the supercell dimensions $((6.0115)_3 Å_3)$ are determined through a cell optimization using a conjugate gradient optimization. Geometry optimization is performed with the Quickstep module utilizing a Broyden–Fletcher–Goldfarb–Shannon (BFGS) optimizer. A maximum force of 24 meVÅ-1 is used as convergence criteria. All atoms in all systems are relaxed.

AIMD is performed in the canonical ensemble, using a CSVR thermostat, which achieves canonical sampling through velocity rescaling.[59] For thermalization and calibration of the thermostat, the time constant of the thermostat is set to 15 fs and the AIMD is run for 1ps. The time constant is then set to 1ps for the remainder of the AIMD. All AIMD steps prior to equilibration of the total energy and temperature (typically ~2ps) are discarded. AIMD time steps of 10fs are used for PbS/Cl, PbS/I, PbS/Br, and bulk, while 1.5fs time steps are employed for the PbS/mth NCs due to the high frequency C-H stretching modes on the mth ligands. AIMD simulations are run for a total of 10-15ps, and all averaged values presented in the manuscript are averaged over the entire AIMD window, barring the first ~2ps which are discarded. We post-process the atom trajectories by removing the 6 macroscopic degrees of freedom (3x translation, 3x rotation) using the Iterative Closest Point algorithm of Besl and McKay.[60]

FSSH-NBRA are performed utilizing QMflows-NAMD [https://github.com/SCM-NV/qmworks-namd] for computation of the non-adiabatic couplings using the molecular orbitals (MOs) generated from CP2K. For these calculations, occupied and virtual MOs are calculated via diagonalization of the Fock matrix generated at each nuclear configuration of

the MD trajectory, utilizing the Broyden mixing method,[61] and a convergence of 10^{-5}. Afterwards, the MOs energies and the non-adiabatic couplings between MOs are printed in a format readable by the PYXAID package,[45] which propagates the carrier dynamics. Electron/hole dynamics are computed independently from one another, fixing one carrier in the HOMO/LUMO. All states within 1eV of the band edge for the relevant cooling carrier are included for each calculation.

We follow the procedure described in our previous work[11] to compute the phonon band structure in Figure SI-1 and the density of states shown in Figure 2c. However, in this work we use a lattice constant value of 6.0115 Å, which is found for bulk PbS via cell optimization in CP2K. More details of the bulk calculations are given in the **Supporting Information**.

ASSOCIATED CONTENT

Supporting Information The Supporting Information is available free of charge via the Internet at http://pubs.acs.org. Bulk PbS phonon bandstructure, electronic bandstructure with and without SO + HF, more analysis of the electronic fine structure of the PbS NCs, figure describing NC construction, phonon density of states for the NCs, and captions for the GIF animations are provided.

Animations animations are available free of charge via the Internet at http://pubs.acs.org. Animations of the time dependent CBM wavefunctions and VBM carrier densities for each of the AIMD simulations is provided.

Corresponding Author

Email: vwood@ethz.ch

REFERENCES

(1)   Boles, M. A.; Ling, D.; Hyeon, T.; Talapin, D. V. The Surface Science of Nanocrystals. *Nat. Mater.* **2016**, *15*, 141–153.

(2)   Reiss, P.; Protière, M.; Li, L. Core/shell Semiconductor Nanocrystals. *Small* **2009**, *5*, 154–168.

(3)   Hines, M. A.; Guyot-Sionnest, P. Synthesis and Characterization of Strongly Luminescing ZnS-Capped CdSe Nanocrystals. *J. Phys. Chem.* **1996**, *100*, 468–471.

(4)   Brovelli, S.; Schaller, R. D.; Crooker, S. A.; García-Santamaría, F.; Chen, Y.; Viswanatha, R.; Hollingsworth, J. A.; Htoon, H.; Klimov, V. I. Nano-Engineered Electron-Hole Exchange Interaction Controls Exciton Dynamics in Core-Shell Semiconductor Nanocrystals. *Nat. Commun.* **2011**, *2*, 280.

(5)   Mews, A.; Eychmüller, A.; Giersig, M.; Schooss, D.; Weller, H. Preparation, Characterization, and Photophysics of the Quantum Dot Quantum Well System CdS/HgS/CdS. *J. Phys. Chem.* **1994**, *98*, 934–941.

(6)   Pandey, A.; Guyot-Sionnest, P. Slow Electron Cooling in Colloidal Quantum Dots. *Science (80-.).* **2008**, *322*, 929–932.

(7)   Klem, E. J. D.; Shukla, H.; Hinds, S.; MacNeil, D. D.; Levina, L.; Sargent, E. H. Impact of Dithiol Treatment and Air Annealing on the Conductivity, Mobility, and Hole Density

in PbS Colloidal Quantum Dot Solids. *Appl. Phys. Lett.* **2008**, *92*, 90–93.

(8)   Liu, Y.; Gibbs, M.; Puthussery, J.; Gaik, S.; Ihly, R.; Hillhouse, H. W.; Law, M. Dependence of Carrier Mobility on Nanocrystal Size and Ligand Length in PbSe Nanocrystal Solids. *Nano Lett.* **2010**, *10*, 1960–1969.

(9)   Ip, A. H.; Thon, S. M.; Hoogland, S.; Voznyy, O.; Zhitomirsky, D.; Debnath, R.; Levina, L.; Rollny, L. R.; Carey, G. H.; Fischer, A.; et al. Hybrid Passivated Colloidal Quantum Dot Solids. *Nat. Nanotechnol.* **2012**, *7*, 577–582.

(10) Brown, P. R.; Kim, D.; Lunt, R. R.; Zhao, N.; Bawendi, M. G.; Grossman, J. C.; Bulovi??, V. Energy Level Modification in Lead Sulfide Quantum Dot Thin Films through Ligand Exchange. *ACS Nano* **2014**, *8*, 5863–5872.

(11) Bozyigit, D.; Yazdani, N.; Yarema, M.; Yarema, O.; Lin, W. M. M.; Volk, S.; Vuttivorakulchai, K.; Luisier, M.; Juranyi, F.; Wood, V. Soft Surfaces of Nanomaterials Enable Strong Phonon Interactions. *Nature* **2016**, *531*, 618–622.

(12) Kagan, C. R.; Lifshitz, E.; Sargent, E. H.; Talapin, D. V. Building Devices from Colloidal Quantum Dots. *Science (80-.).* **2016**, *353*, aac5523-aac5523.

(13) Zherebetskyy, D.; Scheele, M.; Zhang, Y.; Bronstein, N.; Thompson, C.; Britt, D.; Salmeron, M.; Alivisatos, P.; Wang, L.-W. Hydroxylation of the Surface of PbS Nanocrystals Passivated with Oleic Acid. (Suppl Mat). *Science* **2014**, *344*, 1380–1384.

(14) Luther, J. M.; Law, M.; Beard, M. C.; Song, Q.; Reese, M. O.; Ellingson, R. J.; Nozik, A. J. Schottky Solar Cells Based on Colloidal Nanocrystal Films. *Nano Lett.* **2008**, *8*, 3488–3492.

(15) Piliego, C.; Protesescu, L.; Bisri, S. Z.; Kovalenko, M. V.; Loi, M. A. 5.2% Efficient PbS Nanocrystal Schottky Solar Cells. *Energy Environ. Sci.* **2013**, *6*, 3054.

(16) Pattantyus-Abraham, A. G. A.; Kramer, I. J. I.; Barkhouse, A. R.; Wang, X.; Konstantatos, G.; Debnath, R.; Levina, L.; Raabe, I.; Nazeeruddin, M. K.; Grätzel, M.;

et al. Depleted-Heterojunction Colloidal Quantum Dot Solar Cells. *ACS Nano* **2010**, *4*, 3374–3380.

(17)   An, J. M.; Franceschetti, A.; Dudiy, S. V.; Zunger, A. The Peculiar Electronic Structure of PbSe Quantum Dots. *Nano Lett.* **2006**, *6*, 2728–2735.

(18)   Efros, A.; Rosen, M.; Kuno, M.; Nirmal, M.; Norris, D.; Bawendi, M. Band-Edge Exciton in Quantum Dots of Semiconductors with a Degenerate Valence Band: Dark and Bright Exciton States. *Phys. Rev. B. Condens. Matter* **1996**, *54*, 4843–4856.

(19)   Efros, A. L.; Rodina, A. V. Band-Edge Absorption and Luminescence of Nonspherical Nanometer-Size Crystals. *Phys. Rev. B* **1993**, *47*, 10005–10007.

(20)   Reboredo, F. a; Zunger, A. L-X Crossover in CBM of Ge Quantum Dots. *Phys. Rev. B* **2000**, *62*, 2275–2278.

(21)   Voznyy, O.; Fan, F.; Ip, A.; Kiani, A.; Thon, S. M.; Kemp, K. W.; Levina, L.; Sargent, E. H. Passivation-Sensitive Exciton Finestructure Produces Excess Stokes Shifts in Colloidal Quantum Dots. *Math Pubs Sci. Publ. Data* **2016**.

(22)   Cui, J.; Beyler, A. P.; Coropceanu, I.; Cleary, L.; Avila, T. R.; Chen, Y.; Cordero, J. M.; Heathcote, S. L.; Harris, D. K.; Chen, O.; et al. Evolution of the Single-Nanocrystal Photoluminescence Linewidth with Size and Shell: Implications for Exciton-Phonon Coupling and the Optimization of Spectral Linewidths. *Nano Lett.* **2016**, *16*, 289–296.

(23)   Qiao, H.; Abel, K. A.; Van Veggel, F. C. J. M.; Young, J. F. Exciton Thermalization and State Broadening Contributions to the Photoluminescence of Colloidal PbSe Quantum Dot Films from 295 to 4.5 K. *Phys. Rev. B* **2010**, *82*, 1–5.

(24)   Turyanska, L.; Patane, A.; Henini, M.; Hennequin, B.; Thomas, N. R. Temperature Dependence of the Photoluminescence Emission from Thiol-Capped PbS Quantum Dots. *Appl. Phys. Lett.* **2007**, *90*, 1–4.

(25)   Campos, M. P.; Hendricks, M. P.; Beecher, A. N.; Walravens, W.; Swain, R. A.;

Cleveland, G. T.; Hens, Z.; Sfeir, M. Y.; Owen, J. S. A Library of Selenourea Precursors to PbSe Nanocrystals with Size Distributions near the Homogeneous Limit. *J. Am. Chem. Soc.* **2017**, *139*, 2296–2305.

(26) Caram, J. R.; Bertram, S. N.; Utzat, H.; Hess, W. R.; Carr, J. A.; Bischof, T. S.; Beyler, A. P.; Wilson, M. W. B.; Bawendi, M. G. PbS Nanocrystal Emission Is Governed by Multiple Emissive States. *Nano Lett.* **2016**, *16*, 6070–6077.

(27) Besombes, L.; Kheng, K.; Marsal, L.; Mariette, H. Acoustic Phonon Broadening Mechanism in Single Quantum Dot Emission. *Phys. Rev. B* **2001**, *63*, 155307.

(28) Krauss, T. D.; Wise, F. W. Coherent Acoustic Phonons in a Semiconductor Quantum Dot. *Phys. Rev. Lett.* **1997**, *79*, 5102–5105.

(29) McKimmie, L. J.; Lincoln, C. N.; Jasieniak, J.; Smith, T. A. Three-Pulse Photon Echo Peak Shift Measurements of Capped CdSe Quantum Dots. *J. Phys. Chem. C* **2010**, *114*, 82–88.

(30) Schaller, R. D.; Pietryga, J. M.; Goupalov, S. V.; Petruska, M. A.; Ivanov, S. A.; Klimov, V. I. Breaking the Phonon Bottleneck in Semiconductor Nanocrystals via Multiphonon Emission Induced by Intrinsic Nonadiabatic Interactions. *Phys. Rev. Lett.* **2005**, *95*, 1–4.

(31) Cooney, R. R.; Sewall, S. L.; Anderson, K. E. H.; Dias, E. A.; Kambhampati, P. Breaking the Phonon Bottleneck for Holes in Semiconductor Quantum Dots. *Phys. Rev. Lett.* **2007**, *98*, 1–4.

(32) Harbold, J. M.; Du, H.; Krauss, T. D.; Cho, K. S.; Murray, C. B.; Wise, F. W. Time-Resolved Intraband Relaxation of Strongly Confined Electrons and Holes in Colloidal PbSe Nanocrystals. *Phys. Rev. B - Condens. Matter Mater. Phys.* **2005**, *72*, 1–6.

(33) Bozyigit, D.; Lin, W. M. M.; Yazdani, N.; Yarema, O.; Wood, V. A Quantitative Model for Charge Carrier Transport, Trapping and Recombination in Nanocrystal-Based Solar

Cells. *Nat. Commun.* **2015**, *6*, 6180.

(34) Rabouw, F. T.; Vaxenburg, R.; Bakulin, A. a.; Van Dijk-Moes, R. J. A.; Bakker, H. J.; Rodina, A.; Lifshitz, E.; L. Efros, A.; Koenderink, A. F.; Vanmaekelbergh, D. Dynamics of Intraband and Interband Auger Processes in Colloidal Core-Shell Quantum Dots. *ACS Nano* **2015**, *9*, 10366–10376.

(35) Klimov, V. I.; McBranch, D. W.; Leatherdale, C. A.; Bawendi, M. G. Electron and Hole Relaxation Pathways in Semiconductor Quantum Dots. *Phys. Rev. B* **1999**, *60*, 13740–13749.

(36) Wehrenberg, B. L.; Wang, C.; Guyot-Sionnest, P. Interband and Intraband Optical Studies of PbSe Colloidal Quantum Dots. *J. Phys. Chem. B* **2002**, *106*, 10634–10640.

(37) Kilina, S. V; Kilin, D. S.; Prezhdo, O. V. Breaking the Phonon Bottleneck in PbSe and CdSe Quantum Dots : Time- Charge Carrier Relaxation. **2009**, *3*, 93–99.

(38) Kilina, S. V.; Craig, C. F.; Kilin, D. S.; Prezhdo, O. V. Ab Initio Time-Domain Study of Phonon-Assisted Relaxation of Charge Carriers in a PbSe Quantum Dot. *J. Phys. Chem. C* **2007**, *111*, 4871–4878.

(39) Han, P.; Bester, G. Carrier Relaxation in Colloidal Nanocrystals: Bridging Large Electronic Energy Gaps by Low-Energy Vibrations. *Phys. Rev. B - Condens. Matter Mater. Phys.* **2015**, *91*, 1–8.

(40) Liu, J.; Kilina, S. V.; Tretiak, S.; Prezhdo, O. V. Ligands Slow Down Pure-Dephasing in Semiconductor Quantum Dots. *ACS Nano* **2015**, *9*, 9106–9116.

(41) Huang, K.; Rhys, A. Theory of Light Absorption and Non-Radiative Transitions in F-Centres. *Proc. R. Soc. Lond. A. Math. Phys. Sci.* **1950**, *204*, 406–423.

(42) Schaller, R. D.; Klimov, V. I. High Efficiency Carrier Multiplication in PbSe Nanocrystals: Implications for Solar Energy Conversion. *Phys. Rev. Lett.* **2004**, *92*, 186601–1.

(43)   Spoor, F. C. M.; Kunneman, L. T.; Evers, W. H.; Renaud, N.; Grozema, F. C.; Houtepen, A. J.; Siebbeles, L. D. A. Hole Cooling Is Much Faster than Electron Cooling in PbSe Quantum Dots. *ACS Nano* **2016**, *10*, 695–703.

(44)   Spoor, F. C. M.; Tomić, S.; Houtepen, A. J.; Siebbeles, L. D. A. Broadband Cooling Spectra of Hot Electrons and Holes in PbSe Quantum Dots. *ACS Nano* **2017**, *11*, 6286–6294.

(45)   Akimov, A. V.; Prezhdo, O. V. The PYXAID Program for Non-Adiabatic Molecular Dynamics in Condensed Matter Systems. *J. Chem. Theory Comput.* **2013**, *9*, 4959–4972.

(46)   Tully, J. C. Molecular Dynamics with Electronic Transitions. *J. Chem. Phys.* **1990**, *93*, 1061.

(47)   Kilina, S. V.; Kilin, D. S.; Prezhdo, O. V. Breaking the Phonon Bottleneck in PbSe and CdSe Quantum Dots: Time-Domain Density Functional Theory of Charge Carrier Relaxation. *ACS Nano* **2009**, *3*, 93–99.

(48)   Dove, M. T. *Introduction to Lattice Dynamics*; Cambridge University Press, 1993.

(49)   Ridley, B. K. *Quantum Processes in Semiconductors*; Oxford Univ. Press, 1999.

(50)   Somayajulu, G. R. Dependence of Force Constant on Electronegativity, Bond Strength, and Bond Order. VII. *J. Chem. Phys.* **1958**, *28*, 814.

(51)   Zherebetskyy, D.; Zhang, Y.; Salmeron, M.; Wang, L. W. Tolerance of Intrinsic Defects in PbS Quantum Dots. *J. Phys. Chem. Lett.* **2015**, *6*, 4711–4716.

(52)   Cass, L. C.; Malicki, M.; Weiss, E. A. The Chemical Environments of Oleate Species within Samples of Oleate-Coated PbS Quantum Dots. *Anal. Chem.* **2013**, *85*, 6974–6979.

(53)   Kim, D.; Kim, D. H.; Lee, J. H.; Grossman, J. C. Impact of Stoichiometry on the Electronic Structure of PbS Quantum Dots. *Phys. Rev. Lett.* **2013**, *110*, 196802.

(54)   Vandevondele, J.; Krack, M.; Mohamed, F.; Parrinello, M.; Chassaing, T.; Hutter, J.

Quickstep: Fast and Accurate Density Functional Calculations Using a Mixed Gaussian and Plane Waves Approach. *Comput. Phys. Commun.* **2005**, *167*, 103–128.

(55)   Lippert, G.; Hutter, J.; Parrinello, M. A Hybrid Gaussian and Plane Wave Density Functional Scheme. *Mol. Phys.* **1997**, *92*, 477–488.

(56)   Voznyy, O.; Mokkath, J. H.; Jain, A.; Sargent, E. H.; Schwingenschlögl, U. Computational Study of Magic-Size CdSe Clusters with Complementary Passivation by Carboxylic and Amine Ligands. *J. Phys. Chem. C* **2016**, *120*, 10015–10019.

(57)   VandeVondele, J.; Hutter, J. Gaussian Basis Sets for Accurate Calculations on Molecular Systems in Gas and Condensed Phases. *J. Chem. Phys.* **2007**, *127*.

(58)   Hartwigsen, C.; Goedecker, S.; Hutter, J. Relativistic Separable Dual-Space Gaussian Pseudopotentials from H to Rn. *Phys. Rev. B* **1998**, *58*, 3641–3662.

(59)   Bussi, G.; Donadio, D.; Parrinello, M. Canonical Sampling through Velocity Rescaling Polymorphic Transitions in Single Crystals: A New Molecular Dynamics Method Canonical Sampling through Velocity Rescaling. *J. Chem. Phys. J. Appl. Phys. J. Chem. Phys. J. Chem. Phys. J. Chem. Phys. J. Chem. Phys. J. Chem. Phys.* **2007**, *1261*.

(60)   Besl, P.; McKay, N. A Method for Registration of 3-D Shapes. *IEEE Transactions on Pattern Analysis and Machine Intelligence*. 1992, pp 239–256.

(61)   Broyden, C. G. A Class of Methods for Solving Nonlinear Simultaneous Equations. *Math. Comput.* **1965**, *19*, 577–577.
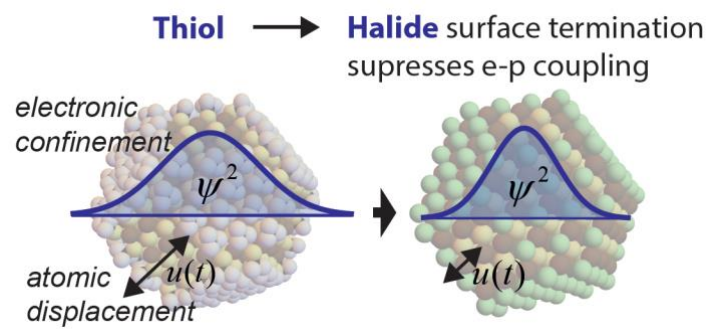
Thiol → Halide surface termination supresses e-p coupling

electronic confinement

ψ^2

atomic displacement $u(t)$

ψ^2

$u(t)$

Table of contents figure

X	$\chi(X)$	IC Pb-X (%)	$n_c[111]$ (e-)		$<u_{[111]}>_2$ ($Å_2$)	A_{ue} ($Å_2$e-)	
			CBM	VBM		CBM	VBM
mth	2.45[HUH]	13.5	0.17	0.27	0.044	0.033	0.043
I	2.66	17.9	0.11	0.18	0.035	0.021	0.024
Br	2.96	23.9	0.10	0.14	0.037	0.019	0.021
Cl	3.16	27.6	0.10	0.11	0.035	0.019	0.020

Table 1. Results for the electronic and phononic properties of the NCs with X-surface terminations. The effective electronegativity of the surface termination X in Pauling units ($\chi(X)$) and the percent ionic character (IC) of the X-Pb bond, computed by the Pauling formula $100(1-exp[-1/4(\chi(X)- \chi(Pb))])$ are given for reference. The total carrier density ($n_c[111]$) on the outer Pb and X atoms on the [111] facet for both bands, and the mean square thermal displacement ($<u_{[111]}>_2$) at 100K of the same atoms are given. In the last column, the computed A_{ue} values (eq. (13)) are shown for both bands at 100K.
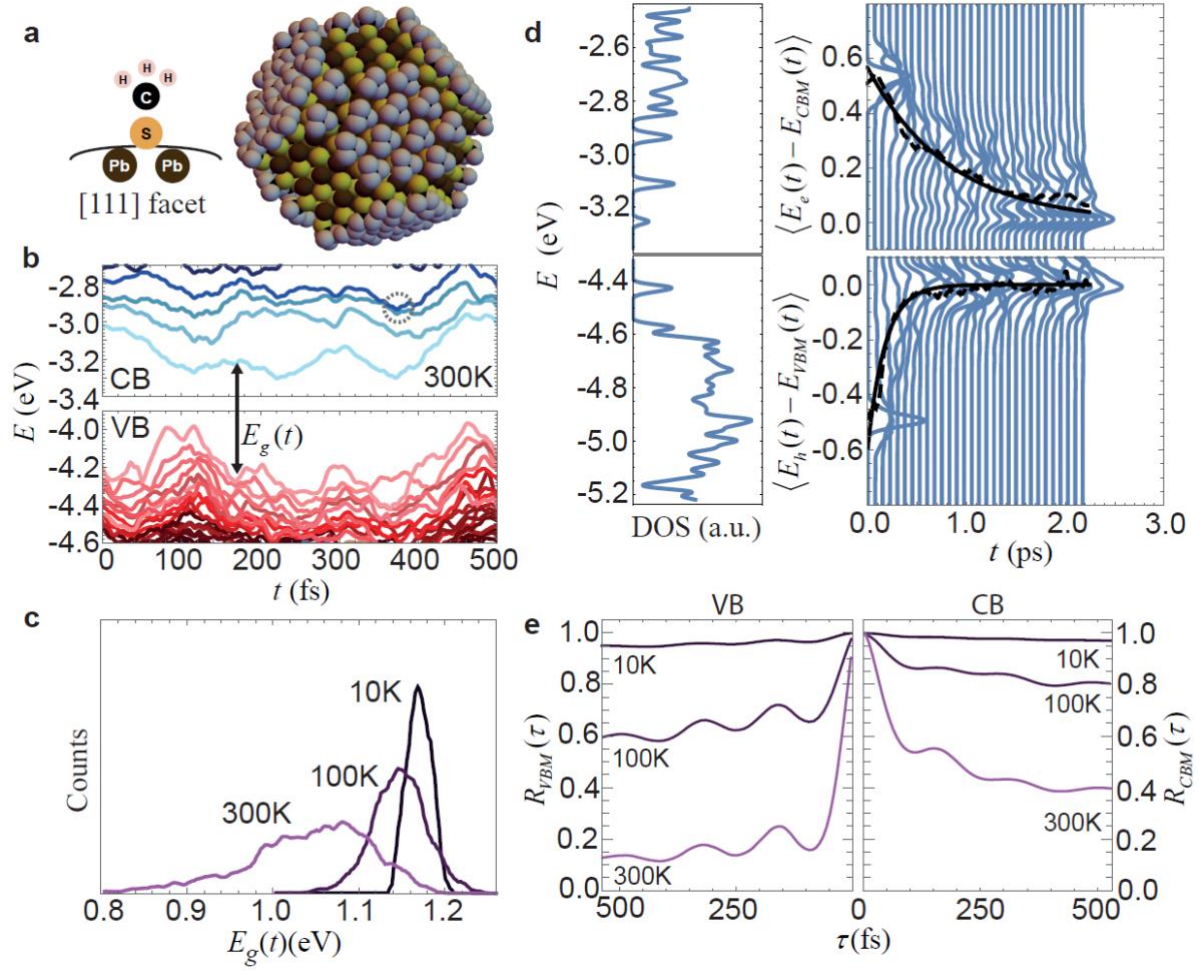
Figure 1 Thermal Broadening and Hot Carrier Cooling in PbS/mth Nanocrystal. a) Atomistic model of a methane thiol-terminated PbS nanocrystal (NC) (PbS/mth) showing bonding of the thiol to the Pb[111] surface. b) Time dependent energies of conduction band (CB) and valence band (VB) states at 300K. The dashed circle indicates an avoided crossing between two states in the CB. c) Histograms showing the band gap energy (E_g) for three different temperatures. d) The density of states of the NC in its nuclear ground state (left). Time dependence of the occupation-weighted density of states (eq. (3)) for an electron and a hole initially excited 0.5eV above the CB minimum or below the VB maximum, respectively (right). e) The wavefunction overlap autocorrelation functions (eq.(8)) for the CB minimum and VB maximum.
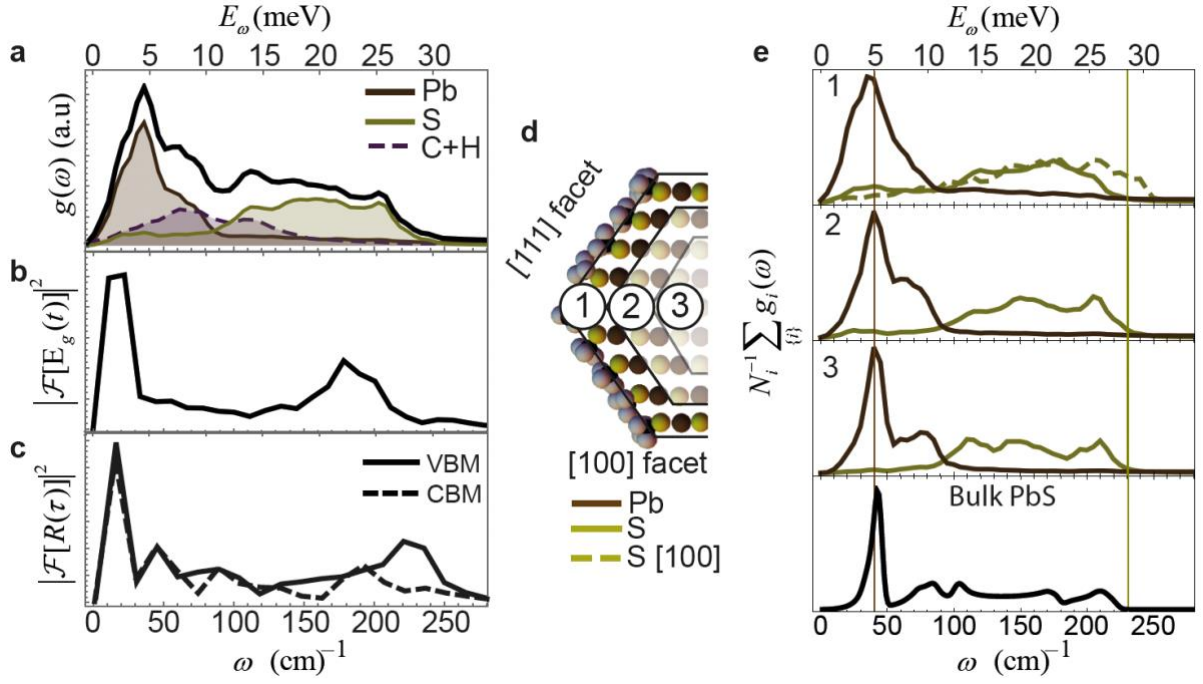
Figure 2. Phonons in the PbS/mth NC and their Coupling to Optical and Electronic Transitions a) Phonon density of states ($g(\omega)$) (black line) for the NC, along with the partial $g(\omega)$ for Pb (brown shading), S (dark yellow shading), and C+H (dashed purple line). b) Power spectra of $E_g(t)$ at 100K. c) Power spectra of the wavefunction overlap autocorrelation functions (eq.(8)) for the CB minimum and VB maximum at 300K. d) Three regions of interest are identified in the NC: the outer Pb and S layer (1), the sub-surface layers (2), and the core (3). The schematic emphasizes the different terminations on [100] and [111] NC facets. e) Partial $g(\omega)$ for Pb (brown line) and S atoms (yellow line) for each of the 3 regions of the NC. The lower panel displays the $g(\omega)$ for bulk PbS.
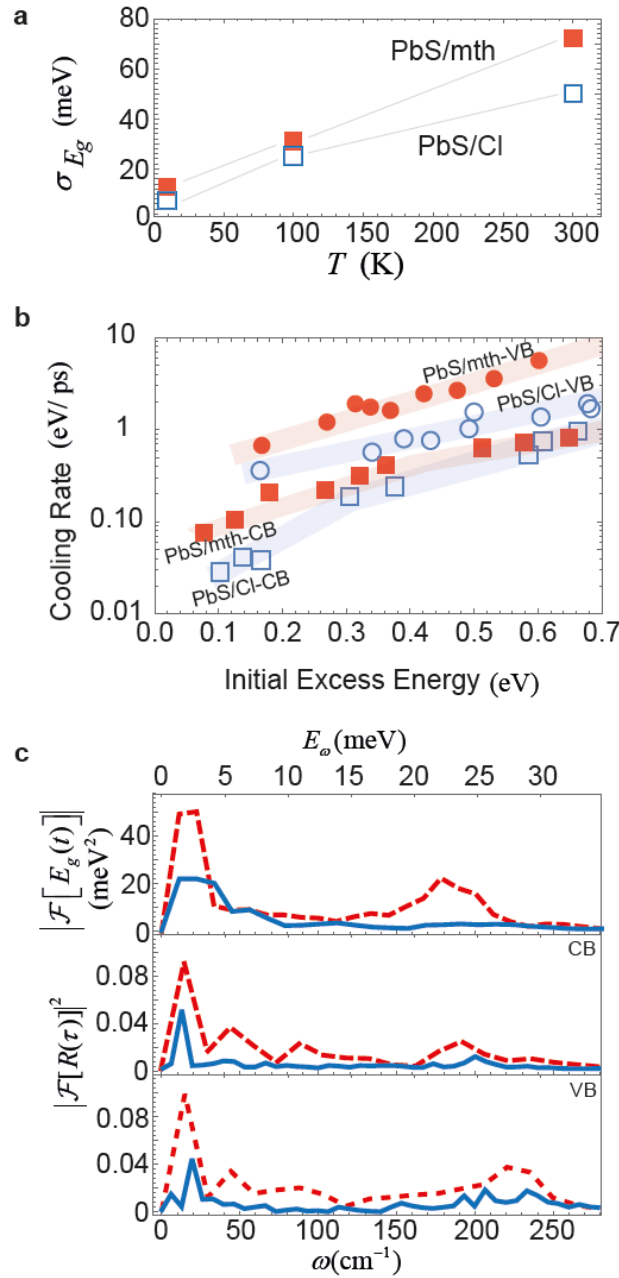
Figure 3. Reducing Electron-Phonon Coupling with Halide Passivation a) Temperature dependent thermal broadening for the PbS/mth (red solid square) and PbS/Cl (blue open square) NCs. Lines between data points are to guide the eye. b) Hot electron (squares) or hole (circles) hot carrier cooling rates associated with the exponential decay of the average excess energy (eq. (4)) for the PbS/mth (solid red) and PbS/Cl (open blue) NCs. Shading is added to guide the eye. c) Power spectra of $E_g(t)$ at 100K (upper panel) and $R(\tau)$ (eq.(8)) for the CBM

and VBM at 300K (lower two panels) for the PbS/Cl NC (solid blue lines) and PbS/mth (dashed red line).
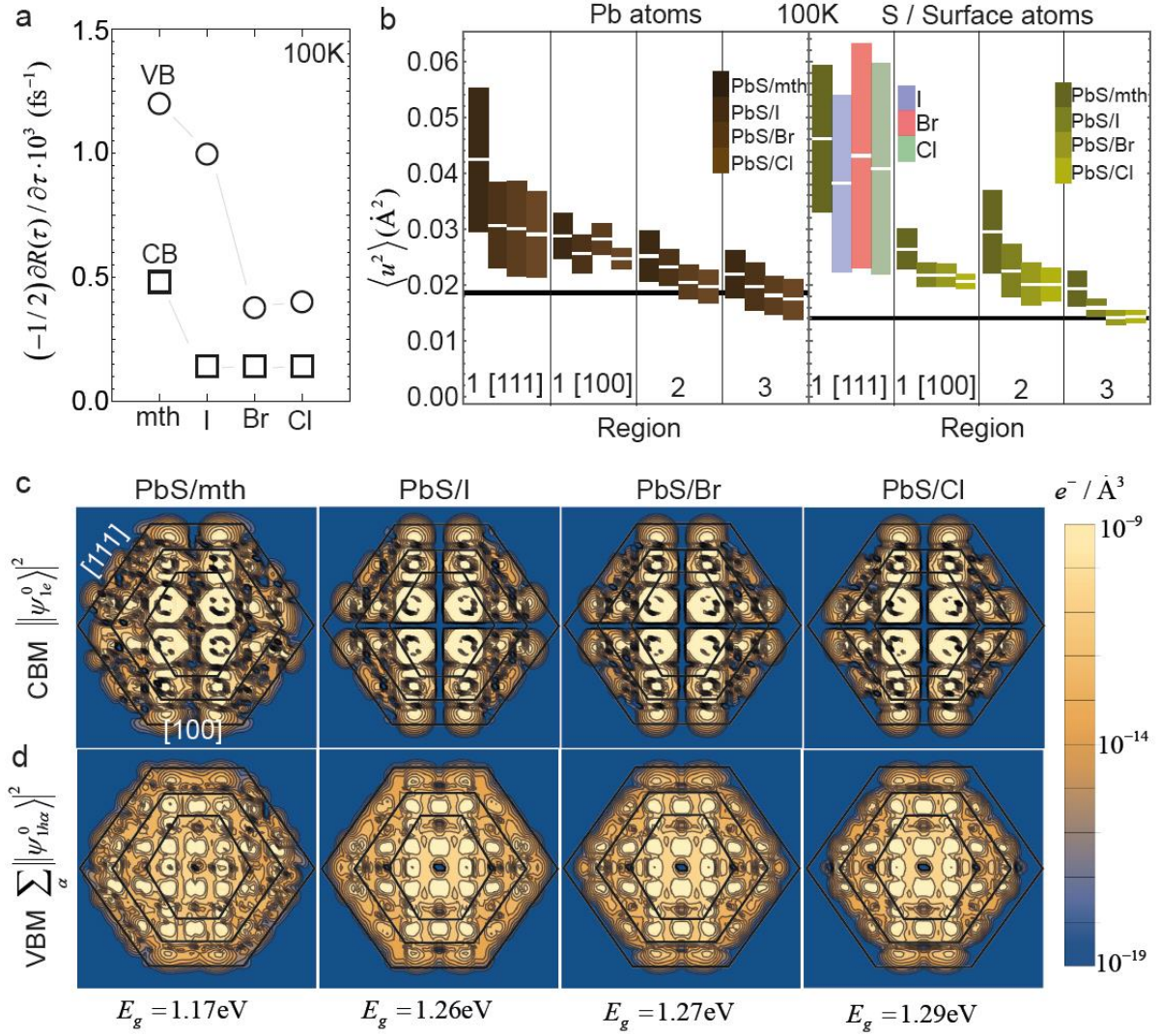
Figure 4 Effects of Halide Termination a) Total couplings (eq. (7)) to all transitions away from the CB minimum (squares) and VB maximum (circles) at 100K for NCs with thiol or halide terminations. b) Plot of mean square thermal displacement $<u_2>$ for Pb (left) and S, I, Br, and Cl atoms (right) in the three regions defined in **Figure 2d**. [111] and [100] facets in Region 1 are plotted separately. The bars represent the range (-σ,+σ). The thick black lines are the $<u_2>$ calculated for Pb and S from bulk PbS. c,d) Slices through a NC showing the electron density in the CB minimum state (c) and the 3-fold degenerate VB maximum states (d) for all four surface terminations: mth, Cl, Br, and Cl. The total electron density per NC is 1. The density plotted for the VB maximum is the average of the three-fold degenerate states $\psi_{1h\alpha}$, while for the CB minimum it is the density in the lowest singly degenerate state ψ_{1e}. The

calculated bandgaps of the NCs (indicated) are underestimated as is typical for density functional theory calculations.
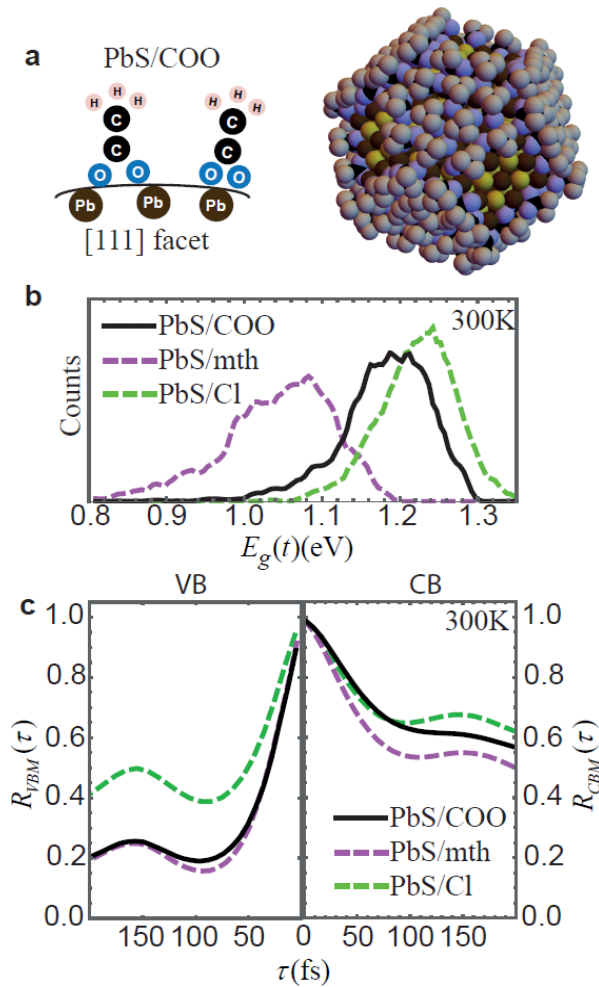
Figure 5 Carboxylate terminated Nanocrystal. a) Atomistic model of a carboxylate-terminated PbS nanocrystal (NC) showing bonding configurations (bridging and chelating bidentate) of the carboxylate to the Pb[111] surface. b) Histograms showing the band gap energy (E_g) at 300K, histograms for the PbS/mth and PbS/Cl are included for reference. c) The wavefunction overlap autocorrelation functions (eq.(8)) for the CB minimum and VB maximum at 300K, plots for PbS/mth and PbS/Cl are included for reference.